

Observation of Arc and Metal Transfer Behavior according to Shielding Gas in the WAAM of Ti–6Al–4V Alloy Using the Pulsed Gas Metal Arc Process

Arc physics, deposition characteristics, and the mechanism of spatter generation were elucidated

BY T. H. LEE, D. H. KAM, J. H. OH, AND C. KIM

Abstract

In arc welding and wire arc additive manufacturing (WAAM) of Ti alloys, pulsed gas metal arc (GMA) processes have a higher deposition than short-circuiting GMA mode processes, such as cold metal transfer, surface tension transfer, and controlled short-circuit processes. In this study, pulsed GMA WAAM of Ti–6Al–4V alloy was conducted under Ar, Ar50%/He50% mixed, and He shielding gases. Owing to the thermionic emission of electrons from the Ti substrate, cathode jets were emitted from the high-temperature region of the weld pool, which interfered with droplet transfer into the weld pool. The arc shape surrounding the droplet varied according to the shielding gas, and the arc was established at the bottom of the hanging droplet under the He shielding gas, which disturbed droplet detachment. Two spatter generation modes of droplet ejection from the weld pool surface and in-flight droplet repelling were observed, and droplet ejection was the most frequent spatter generation mechanism. The mixed shielding gas showed the best performance in terms of arc stability, wire melting, droplet transfer, and spatter suppression. The arc, cathode, and metal transfer characteristics were elucidated in this study, and a suitable gas composition for pulsed GMA WAAM of Ti alloys was proposed.

Keywords

- Wire Arc Additive Manufacturing (WAAM)
- Ti Alloy
- Pulsed Gas Metal Arc

- Shielding Gas
- Cathode Spot
- Wire Melting
- Metal Transfer
- Spatter Generation

Introduction

In the additive manufacturing (AM) of metallic components, wire-based processes have many advantages over powder-based processes. Wire-based AM processes ensure a higher deposition rate, better material efficiency, and reduced surface roughness (Refs. 1, 2), which are indispensable attributes in the AM of large metal products. Laser beams (Ref. 3), electron beams (Ref. 4), and arc plasmas (Ref. 5) have been utilized as heat sources in wire-based AM processes, and wire arc additive manufacturing (WAAM) is popular owing to its flexibility, versatility, and productivity.

Gas tungsten arcs (GTAs), plasma arcs (PAs), and gas metal arcs (GMAs) have been used as electric arcs in WAAM. Among them, GMA WAAM has the highest deposition rate and enables coaxial wire feeding, while GTA and PA WAAM utilize lateral wire feeding (Refs. 6, 7). Therefore, GMA WAAM has been investigated for various metals since the earliest stage of WAAM and was called metal rapid prototyping in its early years (Refs. 8–11).

Titanium alloys have an excellent strength-to-weight ratio and corrosion resistance (Ref. 12); however, their application is limited owing to their high material and processing costs. To overcome the difficulties of conventional Ti alloy processing (such as machining, forming, and welding), AM has been selected as a cost-effective manufacturing process for Ti alloys (Ref. 13). In particular, WAAM is advantageous owing to its high material efficiency in the AM of expensive Ti alloys as well as its high productivity (Ref. 14).

In arc welding and WAAM of Ti alloys, an arc plasma is generated between the anode and cathode, and electrons are

<https://doi.org/10.29391/2023.102.020>

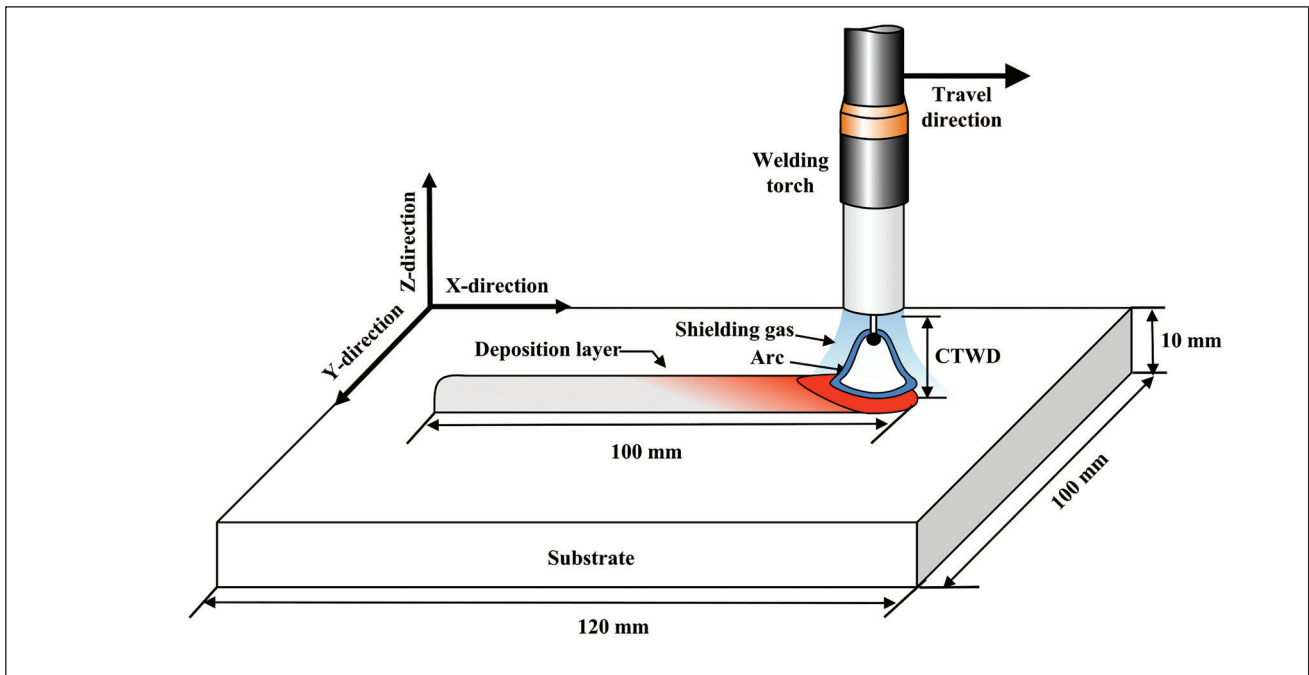


Fig. 1 – Schematic of the experimental setup.

Table 1 – Chemical Compositions of Deposition Wire and Ti-6Al-4V Substrate (wt-%)

Filler Metal: AWS ER Ti-5						
Ti	Al	V	C	Fe	N	O
89.4	6.20	3.95	0.008	0.15	0.001	0.13
Base Metal: Ti-6Al-4V						
Ti	Al	V	C	Fe	N	O
89.0	6.36	3.95	0.011	0.18	0.011	0.01

emitted from the cathode by thermionic emission (Refs. 15, 16). Current density is determined by the cathode's surface temperature, and the cathode spots are concentrated in the relatively high-temperature region. When a Ti alloy substrate is used as the cathode, cathode spots wander on the weld pool, and intense cathode jets from the cathode spots disturb the liquid metal transfer from the anode electrode (Ref. 17).

To minimize the effect of the cathode jet, controlled short-circuit metal transfer modes, such as cold metal transfer (CMT), surface tension transfer (STT[®]), and controlled short-circuit (CSC[™]) processes, have been employed in the GMA WAAM of Ti alloys (Refs. 18–22). However, the deposition rate in the short-circuiting mode is lower than in the pulsed mode or spray transfer mode. To the best of our knowledge, GMA WAAM of Ti alloys using the

pulsed mode or constant-voltage spray transfer mode has not been introduced.

Pulsed gas metal arc welding (GMAW-P) of Ti alloys was conceptualized 40 years ago (Ref. 23), but only a few papers have been published on this topic. Zhang and Li (Ref. 24) proposed an active pulse control technology; however, cathode behavior was not discussed. Shinn et al. (Ref. 25) applied a laser beam to a weld pool, and a cathode spot formed at the laser illumination location by laser heating. Otani (Ref. 26) reported that high-speed torch oscillations could suppress arc wandering. Despite these studies, there is still a need for more-practical solutions.

The shielding gas composition plays a crucial role in electrode melting and metal droplet transfer (Refs. 27, 28), and the He gas (Ref. 26) or Ar-He mixture (Ref. 29) is

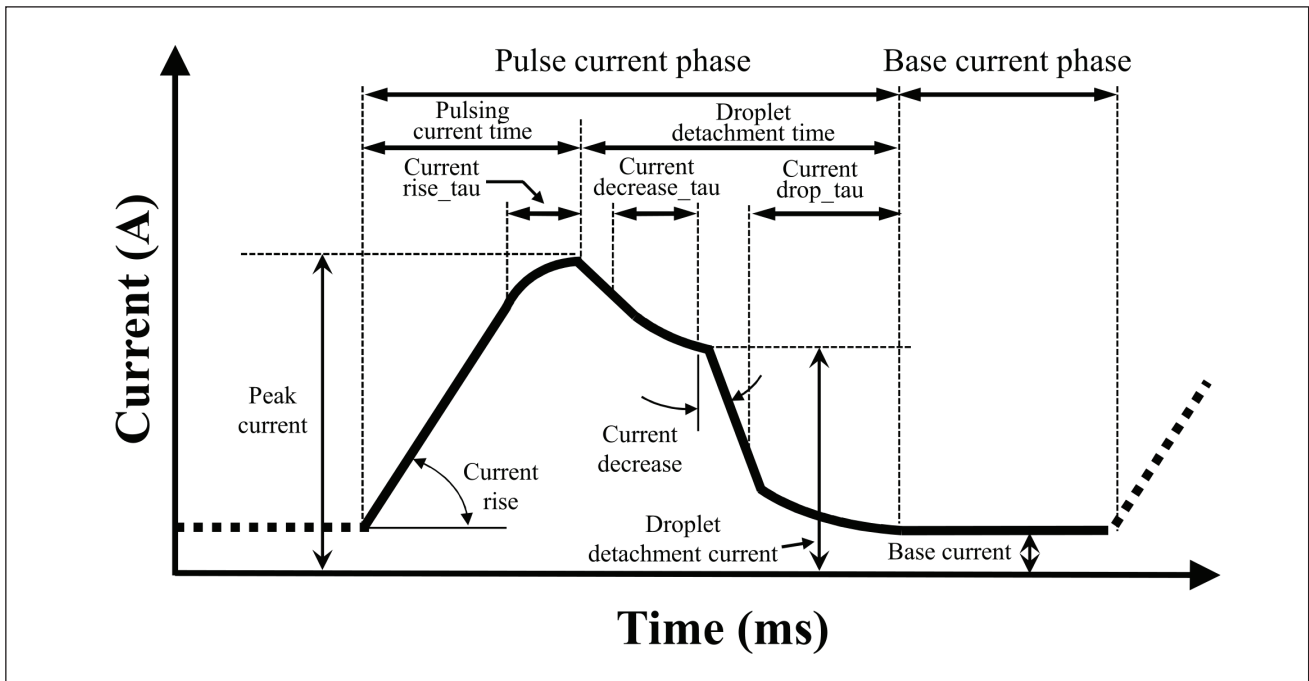


Fig. 2 – Schematic of the pulse current profile.

Table 2 – Pulse Shape Parameters

Parameter	Value
Peak current (I_p)	450.0 A
Base current (I_b)	70.6 A
Droplet detachment current	285.0 A
Pulsing current time	1.6 ms
Droplet detachment time	1.0 ms
Current rise_tau	0.2 ms
Current drop_tau	0.4 ms
Current rise slope	300.0 A/ms
Current decrease slope	500.0 A/ms
Pulsing frequency	123.7 Hz

recommended as the shielding gas in GMAW of Ti alloys. However, the effect of shielding gas composition on GMAW or WAAM has not been fully elucidated.

In this study, the arc and droplet transfer behaviors according to shielding gas composition were investigated using high-speed photography. Ar, Ar 50%/He 50%, and He were supplied as shielding gases, and the arc, cathode, and droplet behaviors were observed. Droplet ejection from the weld pool, rather than in-flight repelling of droplets by the cathode jet, was the more-frequent spatter generation mechanism, and Ar50%/He50% was confirmed as an adequate shielding gas in GMAW-P WAAM of Ti.

Experimental Setup

The overall WAAM setup is illustrated in Fig. 1. The substrate was Ti-6Al-4V alloy plates with a thickness of 10 mm (0.393701 in.), and the welding wire was an AWS ER Ti-5 solid wire with a diameter of 1.2 mm (0.0472441 in.). The substrates were machined to dimensions of 150 × 60 mm (5.90551 × 2.3622 in.), and their surfaces were cleaned by stainless brush grinding and ethanol wiping. The chemical compositions of the substrate and welding wires are listed in Table 1.

A Fronius 3200 CMT (Fronius, Wels, Austria) was used as the arc power source, and the wire was coaxially delivered to the substrate through a wire feeder, torch cable, and deposition torch. The deposition torch was set perpendicular to the substrate, and the filler was deposited with a length of 120 mm (4.72441 in.) along the longitudinal direction. The contact-tip-to-workpiece distance (CTWD) was 15 mm (0.590551 in.). The shielding gas was supplied coaxially through a torch nozzle at a flow rate of 20 L/min. The shielding gas compositions used were Ar 100%, an Ar 50%/He 50%

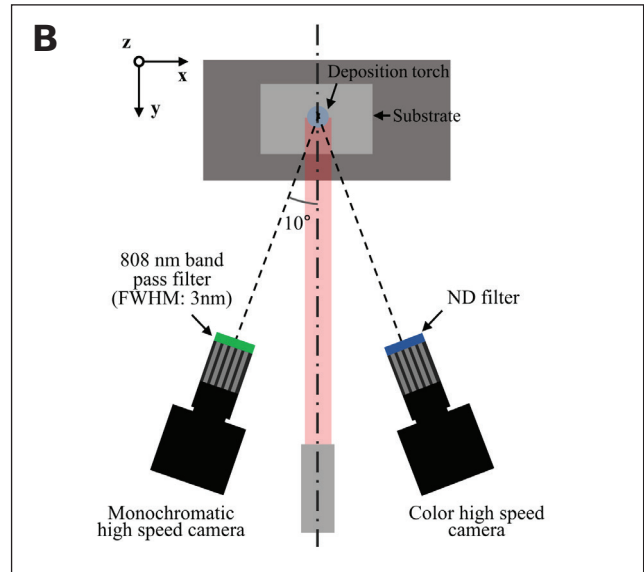
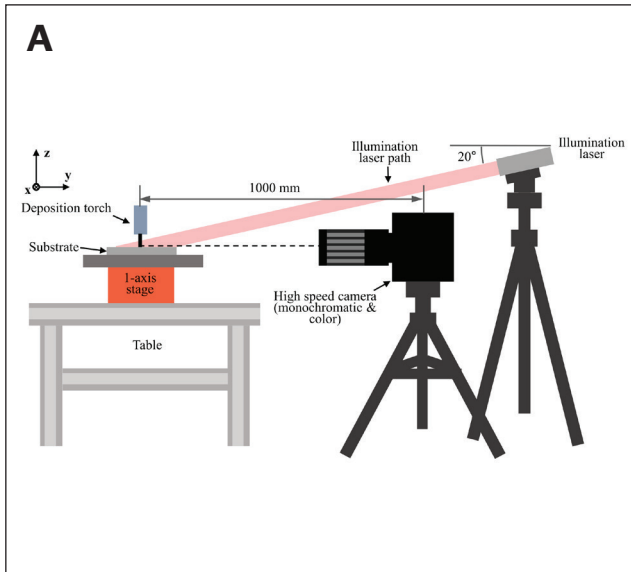
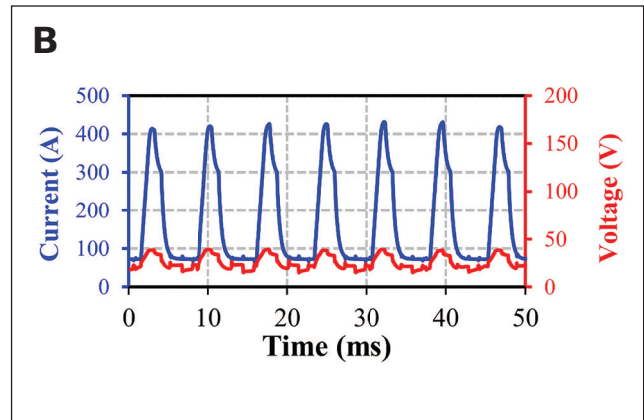
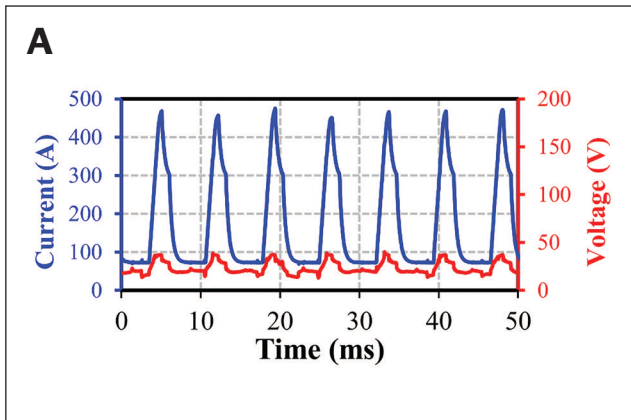


Fig. 3 – Schematic of the high-speed imaging system: A – Arrangement of the welding system, cameras, and illumination laser in the y-z plane; B – arrangement of the high-speed cameras in the x-y plane.



mixture, and He 100%. The purity of the Ar and He gases was 99.999%. The mixed gas was supplied by a gas mixer, MX-3L (Yutaka-Crown, Tokyo, Japan).

The power source generates pulsed current waveforms according to a built-in current profile called a synergic line. The synergic current profiles are programmed to implement one drop transfer per pulse according to the wire feed rate, and the schematic is presented in Fig. 2. For one drop of transfer per pulse, the peak current is set over the transition current, which is a threshold current that enables the spray metal transfer mode while the base-current is set below the transition current. The pulse parameters used in this study are listed in Table 2. The welding wire was deposited under a torch travel speed of 0.5 m/min (1.64042 ft/min) and a wire feed speed of 9.0 m/min (29.5276 ft/min).

Color and monochromatic high-speed cameras were employed to record the arc, wire melting, and cathode spot behaviors. Laser illumination with a wavelength of 808 nm was incorporated in high-speed imaging to minimize the

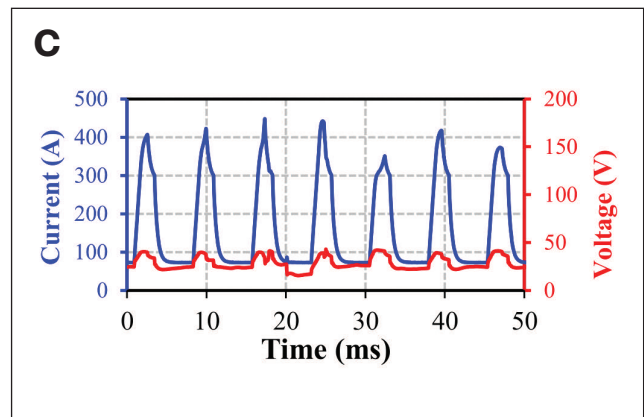


Fig. 4 – Welding current and voltage waveform according to shielding gas: A – Ar; B – Ar/He mixture; C – He.

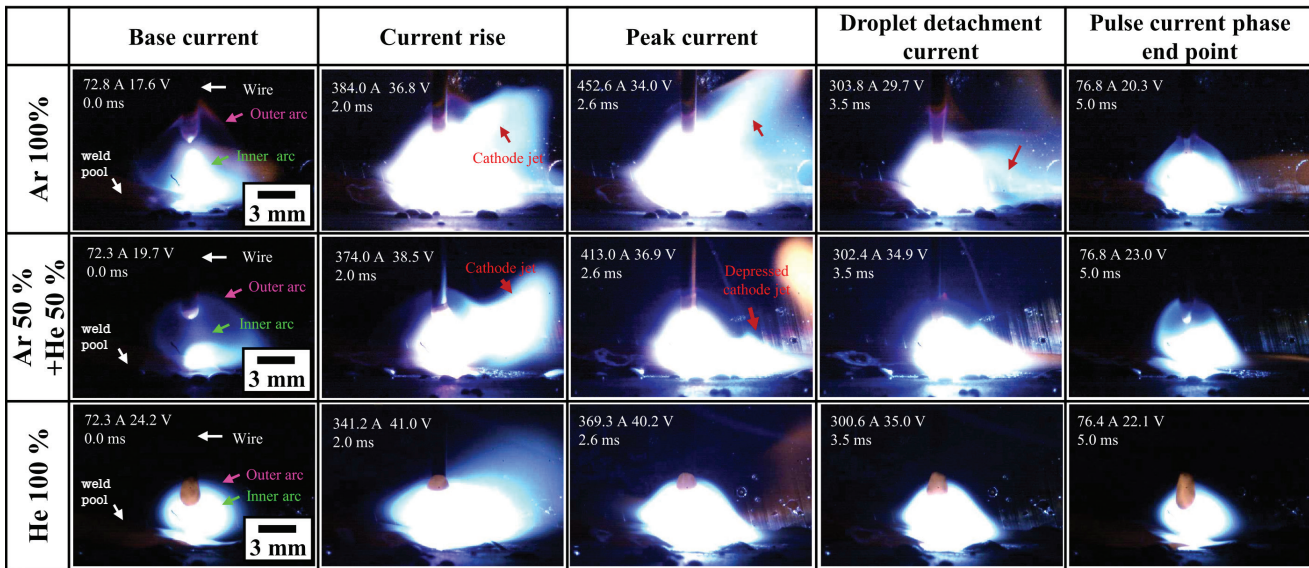


Fig. 5 – Arc plasma behavior recorded using an ND32 filter.

Table 3 – Measured Current and Voltage Waveform Parameters

Parameter	Ar	Ar50%/He50%	He
Average current (A)	173.1	168.1	164.9
Peak current (A)	461.0	416.1	368.3
Standard deviation of peak current (A)	11.3	5.8	49.5
Average voltage (V)	23.3	25.7	26.4
Peak voltage (V)	38.0	39.3	40.4
Standard deviation of peak current (V)	1.3	0.4	1.3

interference of arc light – Fig. 3. The color high-speed camera recorded the arc behavior by adopting proper neutral density (ND) filters, whereas the monochromatic camera recorded the droplet transfer behavior by adopting a band-pass filter with a wavelength of 808 nm and a full width at half maximum (FWHM) of 3 nm. The details of the imaging setup are provided in Ref. 20. The current and voltage waveforms were recorded at a frequency of 50 kHz using an analog-to-digital converter in sync with high-speed imaging.

Results

Arc Behavior

The arc current and voltage waveforms were stable regardless of the shielding gas composition – Fig. 4. The current and voltage waveform characteristics varied according to the shielding gas composition when the same reference pulse profile was selected for all cases. When the pulsing frequency

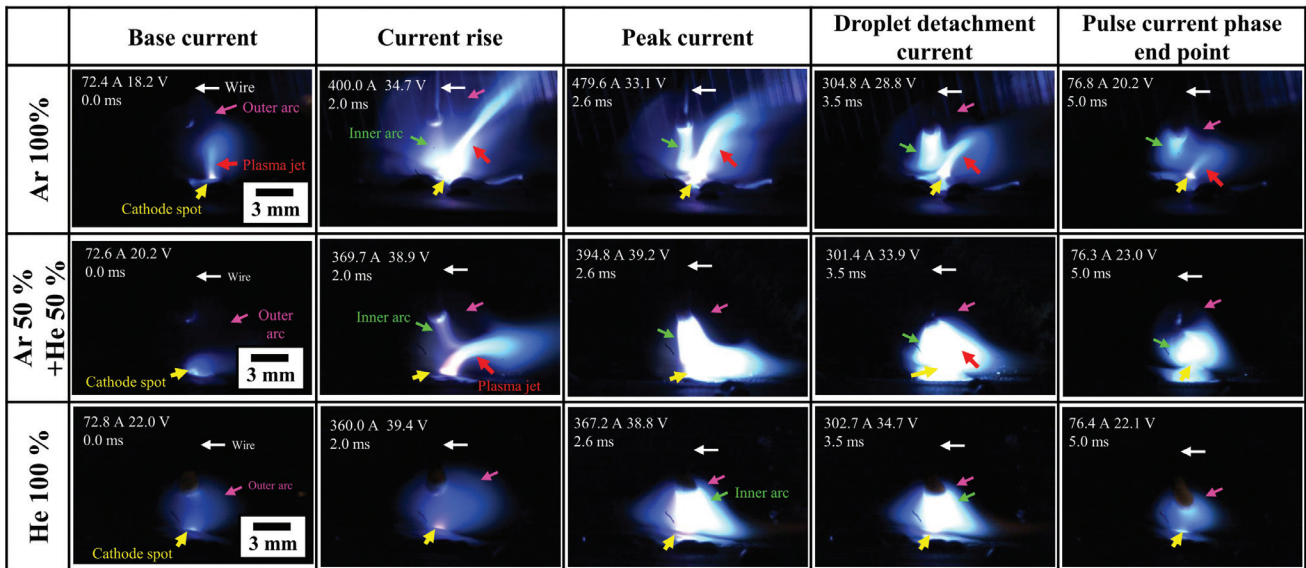
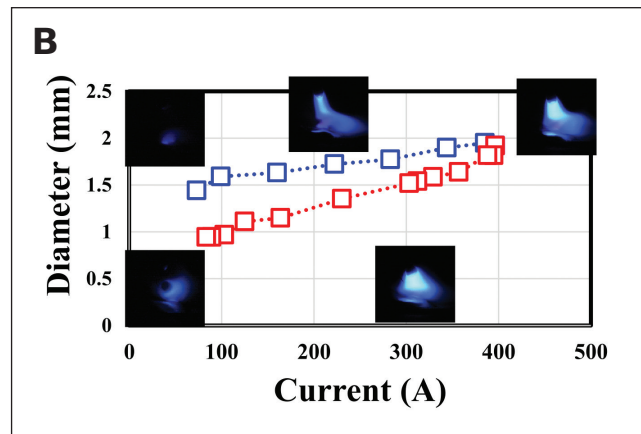
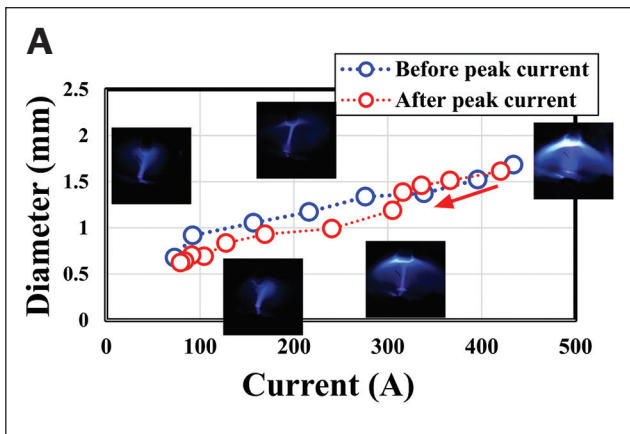


Fig. 6 – Arc plasma behavior recorded using an ND500 filter.



was fixed, the average current decreased and the average voltage increased with increasing He content, which resulted from the decrease in the peak current and the increase in the peak voltage, respectively, as summarized in Table 3. The standard deviations of the peak current and voltage were the lowest for the mixed shielding gas, which indicates that the deposition had the best repeatability under the mixed gas.

The arc plasma behavior was analyzed by high-speed imaging using ND32, ND500, and ND4000 filters – Figs. 5, 6. The ND32, ND500, and ND4000 filters attenuated the inlet light intensity by $1/32$, $1/500$, and $1/4000$, respectively.

The arc plasma consisted of a high-brightness inner region and low-brightness outer region. A bright inner arc was established between the end of the electrode wire and the substrate, and a weak outer arc was connected to the side surface of the electrode and the substrate. Under the Ar shielding gas, the outer arc had a relatively large area, and a considerable distance was observed between the inner and outer arc boundaries. The outer arc region decreased with increasing He content. The arc was more bell-shaped under

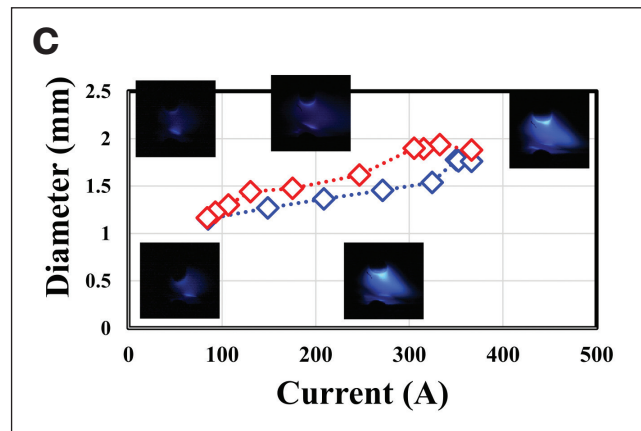


Fig. 7 – Cathode spot diameter in one pulse period according to shielding gas: A – Ar; B – Ar/He mixture; C – He. The diameters were measured from color images recorded using an ND4000 filter.

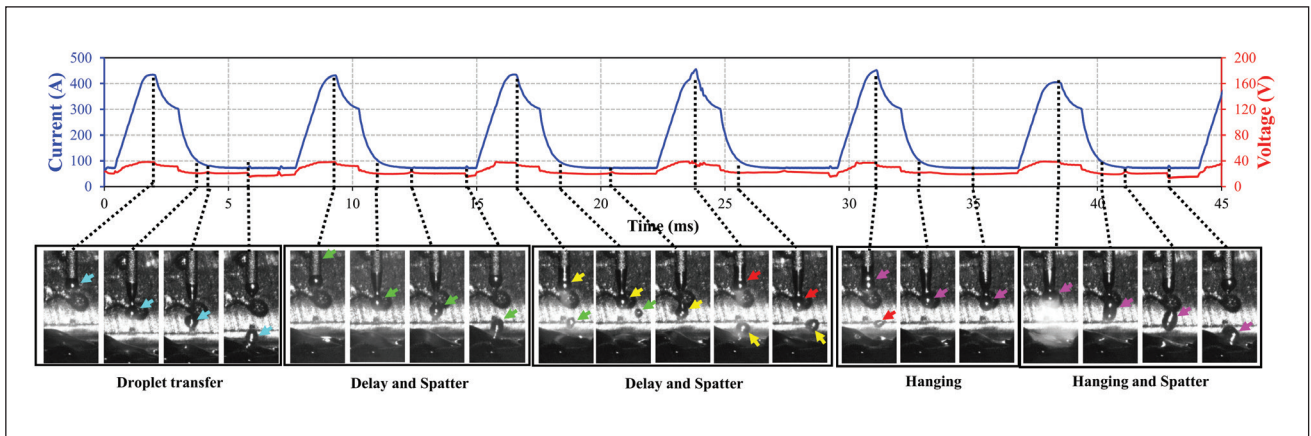


Fig. 8 – Droplet transfer behavior under Ar shielding gas. Arrows indicate droplets for each period.

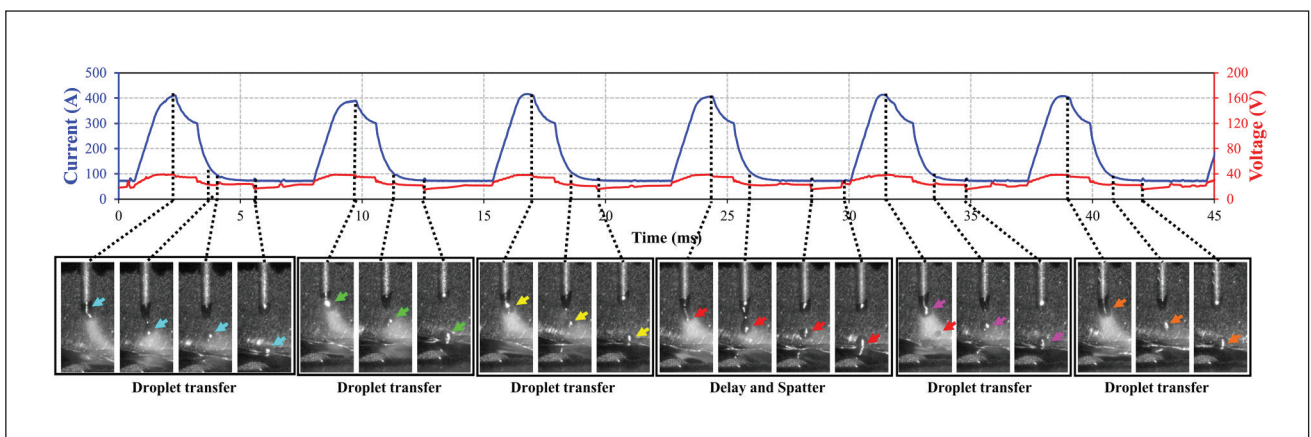


Fig. 9 – Droplet transfer behavior under the mixed shielding gas. Arrows indicate droplets for each period.

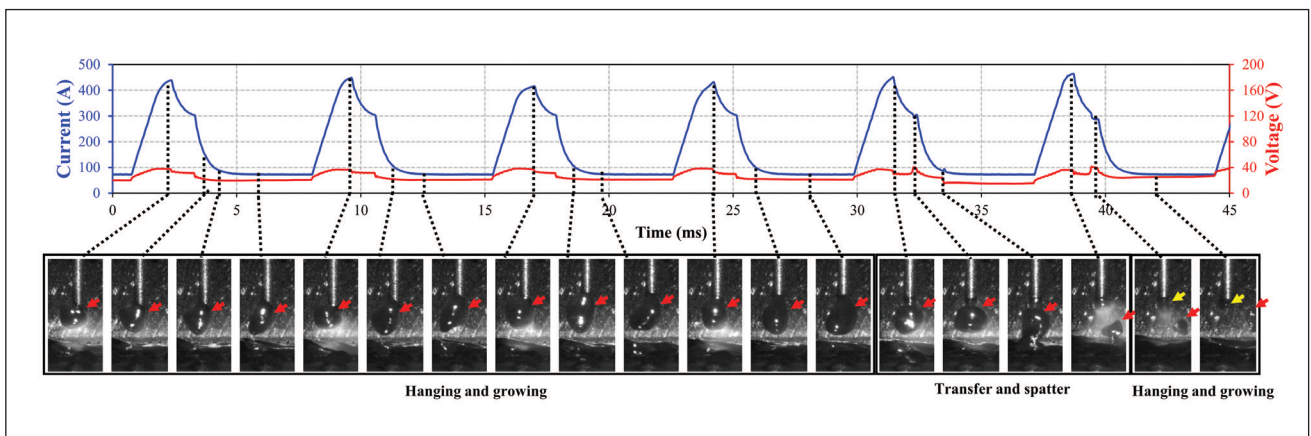


Fig. 10 – Droplet transfer behavior under He shielding gas. Arrows indicate droplets for each period.

Ar shielding gas and more ball-shaped under He shielding gas. These phenomena have been described in previous studies as originating from differences in the ionization voltage, electron-side condensation, and thermal pinch effect (Refs. 16, 27, 30–33).

The intense cathode jets from the substrate were the most critical differences between the arcs of the Ti alloys and other metals – Fig. 6. The cathode jet was generated from the substrate surface and ejected toward the outside of the arc. It was more distinguishable in the Ar-shielding

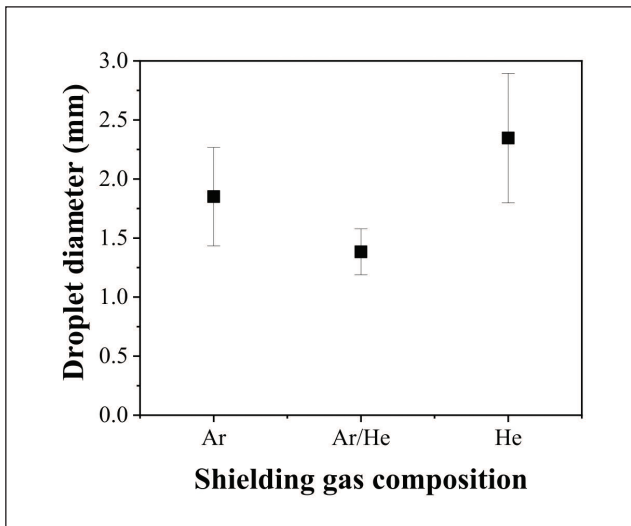


Fig. 11 — Measured droplet diameter according to the shielding gas composition. Error bar indicates the standard deviation.

and high-current phases of the pulse waveform. The cathode jet was not observed during the base-current phase in the ND32-filtered images (Fig. 5) but was found inside the bright inner arc in the ND400-filtered images (Fig. 6). In the pulse-current phase, the intensity of the cathode jet was proportional to the magnitude of the arc current. Under He shielding, no cathode jets were observed outside the arc even at the peak current — Fig. 5. When the cathode jet was weak, it seemed to aim toward the end of the welding wire, as seen in the entire period under the He gas or the low-current durations under the mixed gas.

The cathode spot diameter on the weld pool was measured from the recorded images using an ND filter (ND4000) — Fig. 7. The blue line represents the diameter in the current-increasing phase, and the red line represents the diameter in the current-decreasing phase. The cathode spot diameter was proportional to the arc current but decreased with increasing He content. Interestingly, the cathode spot diameter in the current-increasing phase was higher than that in the current-decreasing phase at the same current magnitude in the Ar and mixed shielding gases, while the opposite was observed for the He shielding gas. Because the cathode spot area is dependent on the high-temperature region on the weld pool surface, the difference in the cathode spot diameter in the increasing and decreasing phases of the current according to the shielding gas originates from the difference in weld pool heating during the pulsing period.

Droplet Transfer

The droplet transfer behavior was recorded using a monochromatic high-speed camera synchronized with current and voltage waveforms.

Figure 8 shows the droplet behavior over six consecutive pulse periods under the Ar shielding gas. The pulse current profile was designed to melt a droplet during the pulse current time and detach the droplets during the droplet detachment

time. The base-current phase was used to maintain a low heat input and prevent the arc from extinguishing. As shown in the first period of Fig. 8, the droplet was formed during the pulse current time and successfully detached from the wire during the droplet detachment time. The detached droplet impinged on the weld pool during the base-current phase, which had the minimum cathode jet intensity. However, in the second to fourth periods, the droplet detached in the base-current phase rather than in the detachment time. In this case, the droplets were transferred into the weld pool during the pulse current phase rather than during the base-current phase and were ejected from the weld pool by the cathode jet. The details of the spatter-generation mechanism are provided in the Spatter Generation section. During the fifth period, no drop per pulse was achieved. The liquid metal was hanging at the end of the welding wire without detachment, and the hanging droplets were detached with a relatively large size in the next period or short-circuited with the substrate, which can generate large spatters.

A stable one-droplet transfer per pulse was observed under the mixed shielding gas — Fig. 9. The droplet size was similar to the wire diameter, and the molten end of the wire was still tapered owing to electron-side condensation (Refs. 34–36). Most droplet detachments from the wire occurred during the droplet detachment time, and the droplets were transferred to the weld pool in the base-current phase. However, in the case where a droplet detached in the base-current phase (the fourth period in Fig. 9), as frequently found under Ar shielding gas (Fig. 8), the delayed transfer caused spattering because the drop contacted the weld pool in the pulse-current phase, which could cause an intense cathode jet. The droplet was then ejected from the weld pool surface and expelled as spatter.

Globular metal transfer was observed under the He shielding gas — Fig. 10. Owing to the high ionization voltage of He, the anode arc was concentrated at the bottom of the hanging droplet, thus exerting an upward force on it. The droplets could not detach during the one pulse period and grew for multiple pulse periods at the wire end. Some droplets detached with a much larger size than the wire and transferred into the weld pool. By contrast, other droplets bridged with the weld pool. That is, they short-circuited and hung at the wire, and spatters were often generated when short-circuiting was broken.

The droplet size was measured for 1.0 s and the average value was plotted with the standard deviation — Fig. 11. Under the mixed shielding gas, the diameter and standard deviation were the minimum. The average diameter was 1.38 mm (0.05433071 in.), slightly higher than the wire diameter, and this method is referred to as the projected (drop) spray transfer mode (Ref. 16). The droplet diameter and standard deviation were the maximum under the He shielding gas. Because the droplet was hanging at the wire end for multiple, variable pulse periods, the droplet size varied, and globular and short-circuit metal transfer modes were inconsistently observed.

The droplet velocity was measured from high-speed images for 1.0 s and plotted with respect to the cathode spot location — Fig. 12. The droplet velocity was classified into four groups according to the phase of the pulse-current

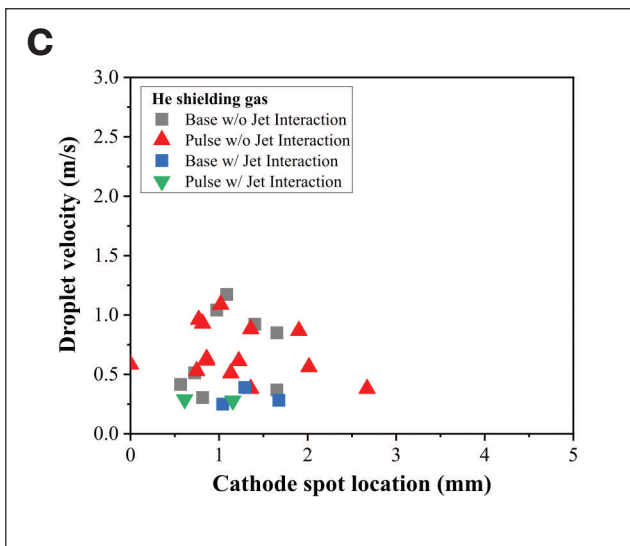
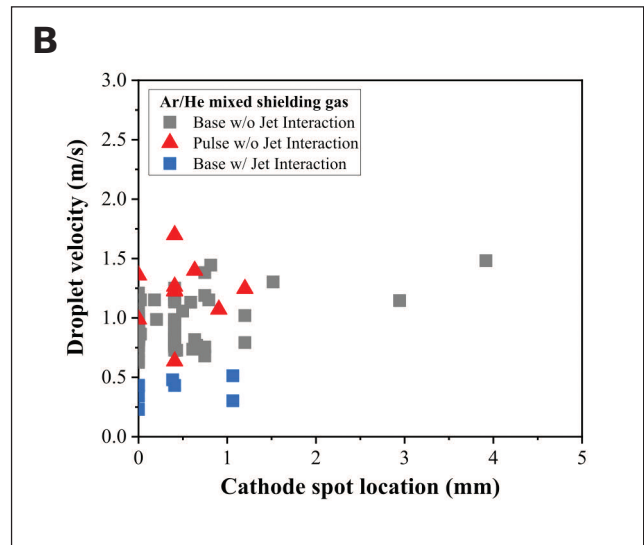
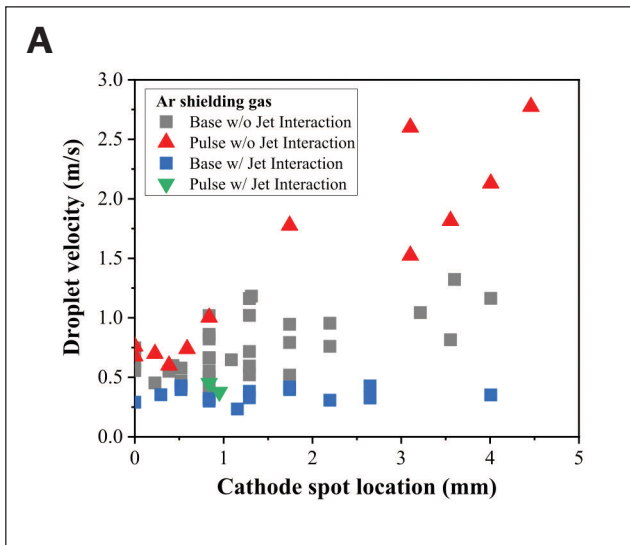


Fig. 12 — Droplet velocity according to cathode spot location, current phase, and cathode jet interaction: A — Ar; B — Ar/He mixture; C — He.

profile and cathode jet interaction. The triangles and squares indicate the pulse and base phases, respectively. The blue and green symbols indicate in-flight droplets interacting with the cathode jet, whereas the gray and red symbols indicate no interaction between the cathode jet and droplet flight. The green triangles represent the droplet velocity in the pulse-current phase when the droplet interacted with the cathode jet.

Under the Ar shielding gas, the cathode spot location varied from the arc center to 4 mm (0.15748 in.), and the droplet velocity increased when the cathode spot moved away from the arc center if the cathode jet did not disturb the droplet flight. Under the mixed shielding gas, cathode spots were located near the arc center, and the interference of the cathode jet on the droplet flight reduced, so only a small number of blue and green symbols were plotted. Under the He shielding gas, the cathode spot location deviated from the

arc center, and the droplet velocity decreased regardless of the cathode spot interaction compared with the other cases.

Spatter Generation

The number of spatters was smallest under the mixed gas, and the worst bead straightness was observed under the He shielding gas — Fig. 13. In addition, the size of the spatter was the largest under the He shielding gas due to the large droplet size, as shown in Figs. 10 and 11.

From the high-speed images, two spatter generation mechanisms were confirmed: droplet ejection from the pool and in-flight repelling.

In the droplet ejection mechanism, when the droplet transferred across the arc column and impinged on the weld pool, the cathode spot abruptly moved to the droplet contact location. Then, an intense cathode jet was generated, which pushed the droplet away from the weld pool and arc plasma boundary — Fig. 14.

In the in-flight repelling mechanism, when the droplet had free flight within the arc column, the cathode jet, generated from the weld pool surface, exerted an upward drag force on the droplet, repelling it from the arc plasma without contacting the weld pool — Fig. 15.

From the high-speed images at 1.0 s, the number of droplets and spatters were counted — Fig. 16. Because the pulsing frequency of the power source was 123.7 Hz (Table 3), nearly one drop per pulse was implemented under the mixed shielding gas, and more than six pulse periods, on average, were necessary to make a droplet under the He shielding. In contrast, the spatter generation frequency under the mixed shielding gas was only 50% higher than that under the He shielding gas. The ratio of spatter to droplets was 12.8% and 64.4% for the mixed and He shielding gases, respectively. The number of spatters owing to in-flight droplet repelling was 10 and 3 under the Ar and mixed shielding gases, respectively, and no in-flight repelling was observed under the He shielding gas, where relatively short arc lengths and large droplets were observed. The ratio of in-flight repelling

spatter to the total spatter was 38.4% and 20.9% for the Ar and mixed shielding gases, respectively.

Discussion

Based on the observations in the Results section, the arc and cathode spot behavior, droplet transfer, and spatter generation mechanism according to the shielding gas composition are discussed in this section.

Arc stability and repeatability were confirmed from the current and voltage waveforms. The standard deviations of the peak current and voltage were highest under the He shielding gas because of inconsistent droplet transfer (Table 1 and Fig. 10). In the high-speed images, the droplet per pulse ratios were 41.2%, 90.0%, and 12.1% for the Ar, mixed gas, and He shielding gas, respectively (Fig. 16), and arc length variation per pulse period was found in the He shielding gas (Fig. 10). The arc was the most stable under the mixed shielding gas, which had the minimum standard deviation of the peak current and voltage, nearly one droplet transfer per pulse, stable impinging of the transferred droplet into the weld pool, and constant arc length.

Distinct differences in the cathode spot and cathode jet behaviors were observed depending on the shielding gas. Under the Ar shielding, the most intense cathode jet was ejected from the weld pool surface, and it was clearly observed even outside the arc plasma (Figs. 5, 6) (Ref. 17). By adding He, the intensity of the cathode jet decreased, and the cathode jet was buried inside the arc plasma under the

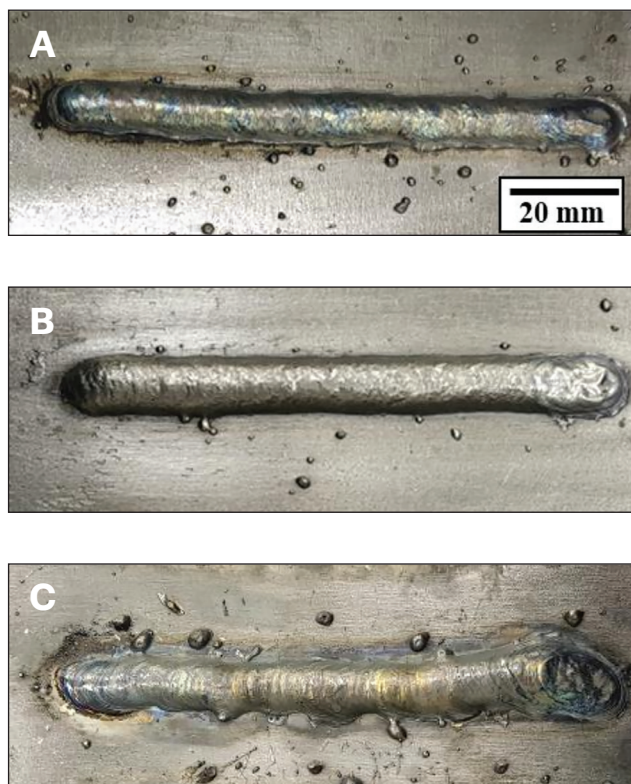


Fig. 13 — Bead appearance according to shielding gas: A — Ar; B — Ar/He mixture; C — He.

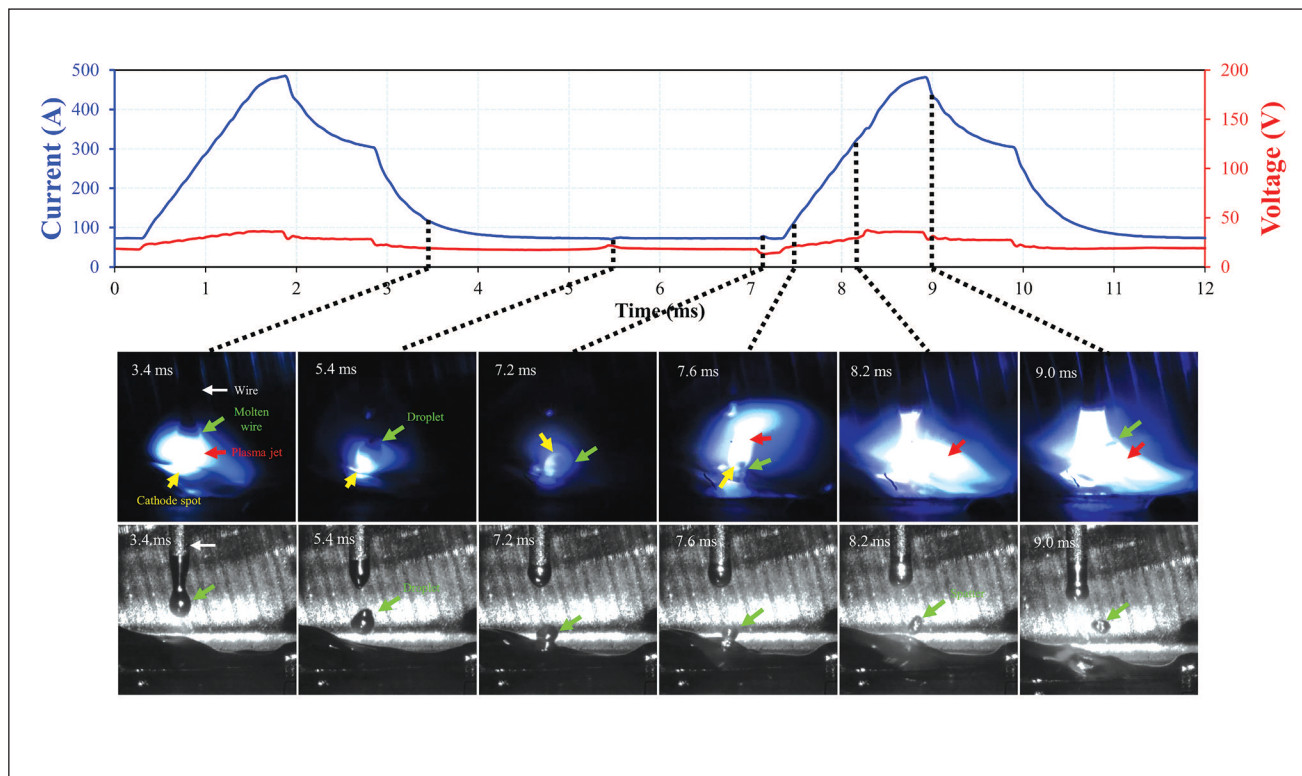


Fig. 14 — Droplet ejection from the weld pool surface under Ar 100%.

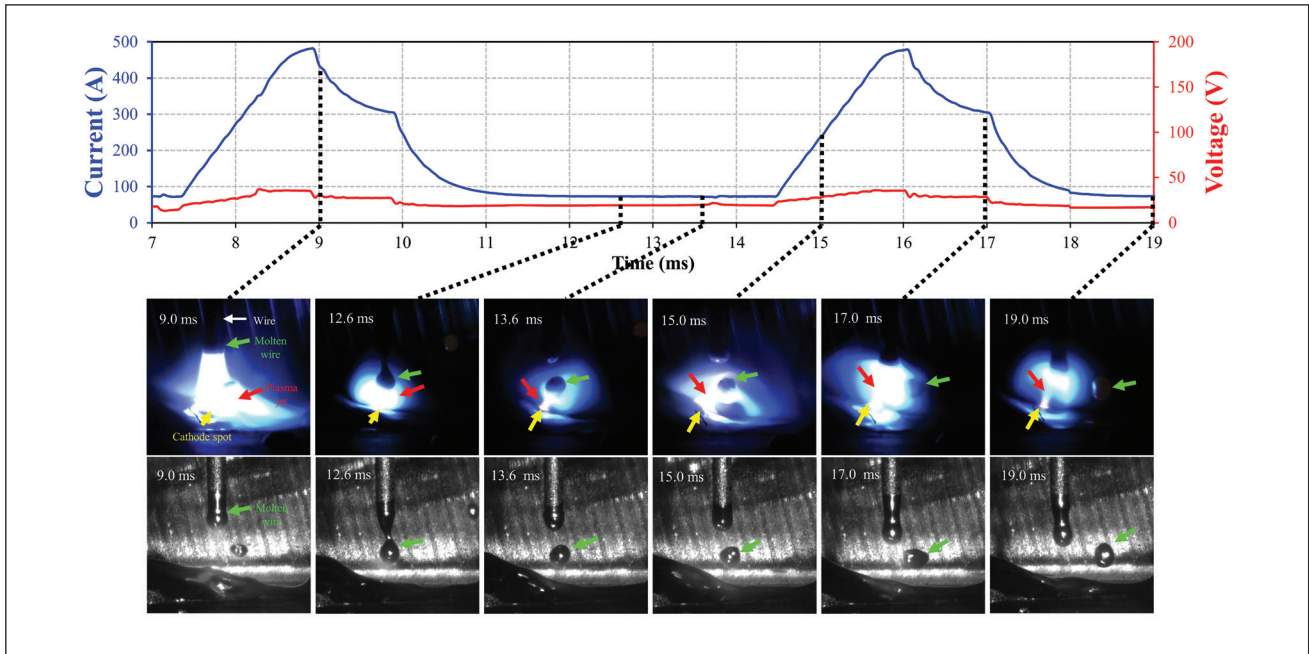


Fig. 15 – In-flight droplet repelling in the arc column under Ar 100%.

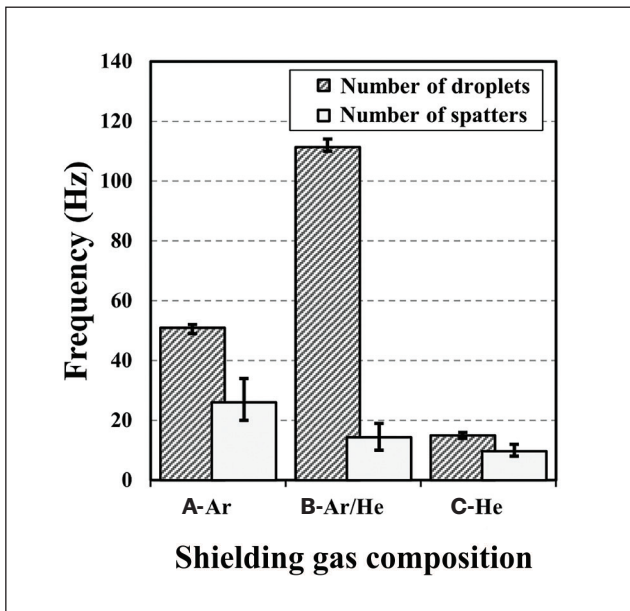


Fig. 16 – The number of droplets transferred according to shielding gas: A – Ar; B – Ar/He mixture; C – He. The error bars show the min-max values.

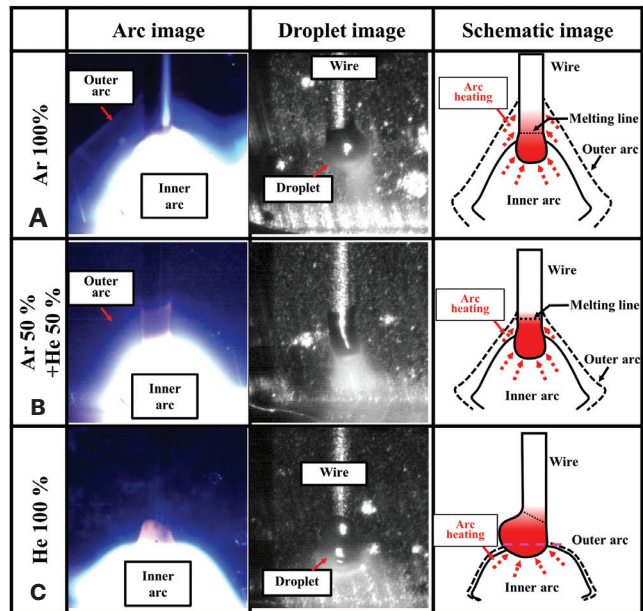


Fig. 17 – Anode phenomena according to shielding gas: A – Ar; B – Ar/He mixture; C – He.

He shielding gas (Ref. 19). The cathode spots were spread between the center and a distance of 4 mm under the Ar shielding gas but were more focused toward the arc center under the mixed shielding gas. Under the He shielding gas, the center of the cathode spot distribution deviated from the arc center (Fig. 12). The cathode spot area increased with the addition of He (Fig. 7) because the Ar plasma transferred more-concentrated heat into the substrate, whereas the He

plasma provided wide and uniform heating into the substrate (Refs. 31, 35, 37).

The different ionization potentials and anode behaviors of the Ar and He gases caused differences in wire melting and droplet detachment behavior – Fig. 17. Under the Ar shielding gas, electrons condensed onto the side surface of the wire, a clear outer arc was observed outside the intense inner arc, and small droplets formed owing to the electromagnetic

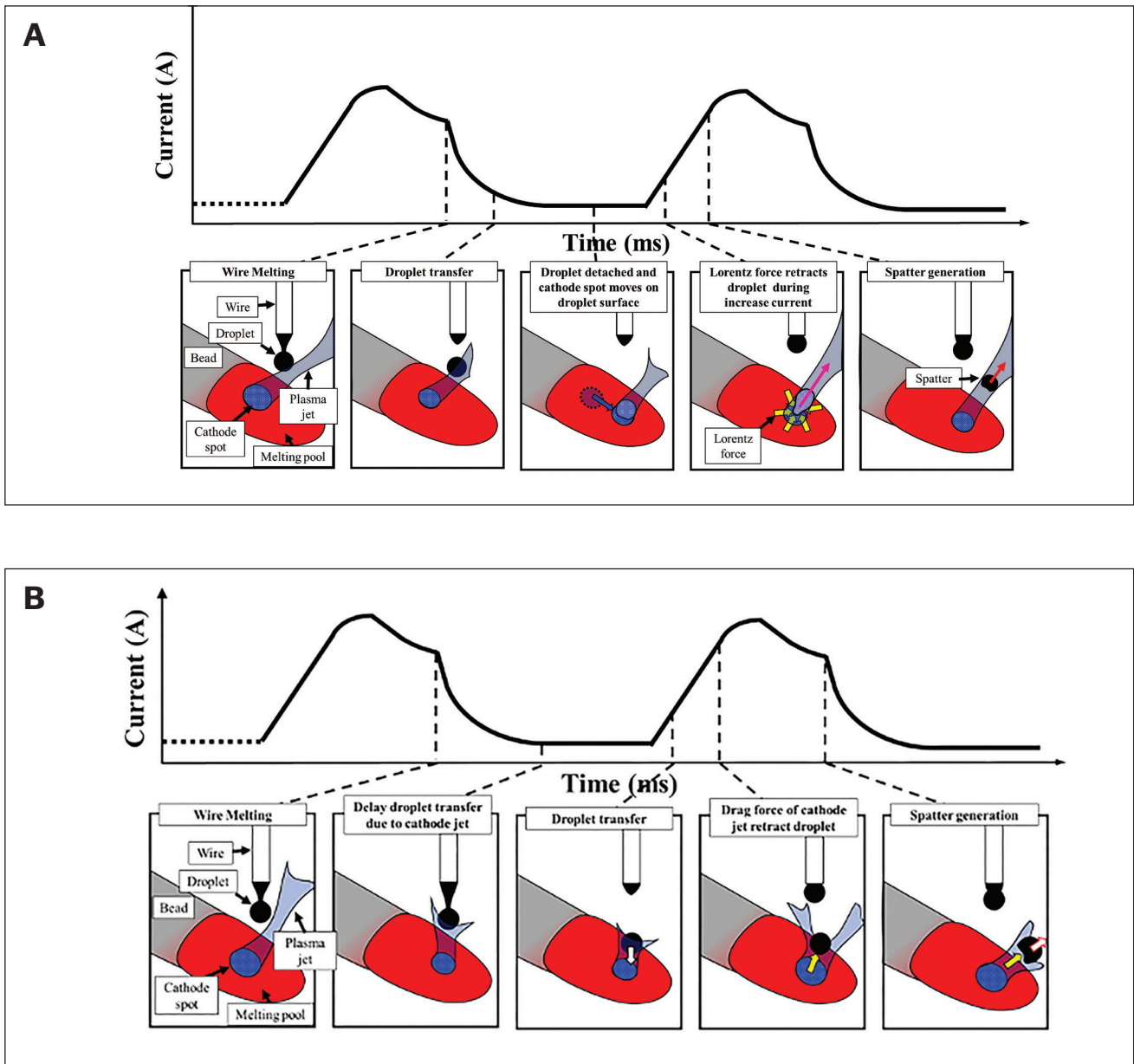


Fig. 18 – Spattering mechanism: A – Lorentz force; B – drag force.

pinch effect. The molten metal tended to hang at the end of the wire in tapered and elongated form, which interfered with the droplet detachment (Refs. 27, 28), and the droplet diameter was 1.5 times the wire diameter – Fig. 11. Under the mixed shielding gas, the droplet diameter was nearly the same as the wire diameter (Fig. 11), and one drop per pulse was implemented at 90% of the pulse period – Fig. 16. In pure He shielding gas, owing to the high ionization voltage, the current path was established from the bottom of the hanging droplet to the substrate without the current path onto the side surface of the wire (Refs. 34, 35), which exerted an upward force and hindered droplet detachment. Thus, the droplet had twice the wire diameter (Fig. 11), and sometimes short-circuiting occurred owing to the large hanging droplets.

After detachment from the wire, the droplets accelerated into the arc column. The drop velocity increased with increas-

ing Ar content in the shielding gas as long as the cathode jet did not interfere with the movement. When the cathode jet exerted upward drag force on the droplet, the velocity of the drop was between 0.2 m/s (7.87402 in./s) and 0.5 m/s (19.685 in./s) regardless of the shielding gas composition – Fig. 12.

Spattering was caused by Lorentz force on the weld pool and drag force on the in-flight droplet – Fig. 18. Lorentz force-driven spattering occurs under the following condition: When the droplet impinges on the surface of the weld pool, droplet heating must increase the local temperature of the weld pool to a sufficient extent to generate a cathode jet, and the arc current must also be sufficiently high to emit an intense cathode jet. Drag force-driven spattering occurs when the droplet interacts with the cathode jet in its trajectory. The dominant spatter generation mechanism in Ti

GMA WAAM is Lorentz force–driven spattering. The ratios of spatter to droplets were 51.0%, 12.9%, and 64.4% for the Ar, the mixed, and the He shielding gas, respectively — Fig. 16. In particular, under the He shielding gas, only Lorentz force–driven spattering was observed, and large hanging droplets caused large spatters, which deteriorated the deposition surface quality by the wandered bead — Fig. 13.

From arc stability, droplet transfer, and spattering behavior, the Ar 50%/He 50% mixed gas showed the best performance in the pulsed GMA WAAM of Ti alloys. The pulsed GMA process had a higher wire melting efficiency than short circuit–based GMA processes, and pulsed GMA processes have great potential for the WAAM of Ti alloys.

Conclusion

In this study, the arc, cathode, and droplet transfer behaviors in the WAAM of Ti alloys using GMAW-P were visualized according to the shielding gas composition. Monochromatic and color high-speed photography were employed in sync to measure arc current and voltage waveforms. Consequently, the following conclusions were drawn:

1. The Ar 50%/He 50% mixed gas showed the best arc stability and droplet transfer characteristics. One droplet per pulse was implemented at 90% of the pulse period, and the cathode spots were relatively concentrated near the arc center. The spatter-to-droplet ratio was 12.9% for the Ar 50%/He 50% mixed gas, whereas the ratios for the Ar and He shielding gases were 51.0% and 64.4%, respectively.

2. An intense cathode jet was observed under the Ar shielding gas, and the intensity decreased with increasing He content. The cathode jet was observed even outside the arc plasma under Ar shielding and high-current conditions. The intense cathode jet exerted an upward force on the droplet when it contacted the weld pool or flowed through an arc column.

3. Under the He shielding gas, a large droplet formed, and the cathode spots deviated from the arc center, which caused the wandered deposit and large spatters to adhere to the substrate. Although He shielding gas has been recommended for GMAW of Ti alloys in some studies, it should be avoided in pulsed GMA WAAM of Ti alloys.

4. Two mechanisms in the spatter generation were observed: molten metal ejection from the weld pool surface by the Lorentz force and in-flight repelling of droplets by the drag force due to the cathode jet. Molten metal ejection, rather than in-flight repelling, played a greater role in spatter generation during pulsed GMA WAAM of Ti alloys.

In this study, the arc physics and deposition characteristics in high-productivity pulsed GMA WAAM of Ti alloys and the mechanism of spatter generation were elucidated according to the shielding gas. Future work will involve multilayer deposition and evaluation of deposition quality and productivity.

Declaration of Competing Interest

The authors declare they have no known competing financial interests or personal relationships that could have appeared to influence the work reported in this paper.

Acknowledgment

This study was carried out with the generous support of the Korea Institute of Industrial Technology under the project “Development of intelligent root technology with add-on modules (KITECH EO-23-0007).”

References

1. Syed, W. U. H., Pinkerton, A. J., and Li, L. 2005. A comparative study of wire feeding and powder feeding in direct diode laser deposition for rapid prototyping. *Applied Surface Science* 247(1–4): 268–276. DOI: 10.1016/j.apsusc.2005.01.138
2. Ahn, Y.-N., and Kim, C. 2013. Comparison of powder feeding and wire feeding in laser cladding. *Journal of Welding and Joining* 31(4): 13–16. DOI: 10.5781/KWJS.2013.31.4.13
3. Kam, D.-H., Kim, Y.-M., and Kim, C. 2016. Recent studies of laser metal 3D deposition with wire feeding. *Journal of Welding and Joining* 34(1): 35–40. DOI: 10.5781/JWJ.2016.34.1.35
4. Gockel, J., Beuth, J., and Taming, K. 2014. Integrated control of solidification microstructure and melt pool dimensions in electron beam wire feed additive manufacturing of Ti-6Al-4V. *Additive Manufacturing* 1–4: 119–126. DOI: 10.1016/j.addma.2014.09.004
5. Williams, S. W., Martina, F., Addison, A. C., Ding, J., Pardal, G., and Colegrove, P. 2016. Wire + arc additive manufacturing. *Materials Science and Technology* 32(7): 641–647. DOI: 10.1179/1743284715Y.0000000073
6. Tabernero, I., Paskual, A., Álvarez, P., and Suárez, A. 2018. Study on arc welding processes for high deposition rate additive manufacturing. *Procedia CIRP* 68: 358–362. DOI: 10.1016/j.procir.2017.12.095
7. Norrish, J., Polden, J., and Richardson, I. 2021. A review of wire arc additive manufacturing: Development, principles, process physics, implementation and current status. *Journal of Physics D: Applied Physics* 54(47): 473001. DOI: 10.1088/1361-6463/ac1e4a
8. Ribeiro, F., Ogunbiyi, B., and Norrish, J. 1997. Mathematical model of welding parameters for rapid prototyping using robot welding. *Science and Technology of Welding and Joining* 2(5): 185–190. DOI: 10.1179/stw.1997.2.5.185
9. Kim, C. H., Na, S. J., and Norrish, J. 1999. Development of metal based rapid prototyping by using GMA welding processes. *Journal of Korean Welding Society* 17(3): 13–16.
10. Zhang, Y. M., Li, P., Chen, Y., and Male, A. T. 2002. Automated system for welding-based rapid prototyping. *Mechatronics* 12(1): 37–53. DOI: 10.1016/S0957-4158(00)00064-7
11. Zhang, Y., Chen, Y., Li, P., and Male, A. T. 2003. Weld deposition-based rapid prototyping: A preliminary study. *Journal of Materials Processing Technology* 135(2–3): 347–357. DOI: 10.1016/S0924-0136(02)00867-1
12. ASM Handbook Committee. 1992. *ASM Handbook, Vol. 2: Properties and Selection: Nonferrous Alloys and Special-Purpose Materials*. Materials Park, Ohio: ASM International. DOI: 10.31399/asm.hb.v02.9781627081627
13. Dutta, B., and Froes, F. H. 2017. The additive manufacturing (AM) of titanium alloys. *Metal Powder Report* 72(2): 96–106. DOI: 10.1016/j.mprp.2016.12.062
14. Cunningham, C. R., Flynn, J. M., Shokrani, A., Dhokia, V., and Newman, S. T. 2018. Invited review article: Strategies and processes for high quality wire arc additive manufacturing. *Additive Manufacturing* 22: 672–686. DOI: 10.1016/j.addma.2018.06.020
15. Guile, A. 1971. Arc-electrode phenomena. *Proceedings of the Institution of Electrical Engineers* 118(9R): 1131–1154. DOI: 10.1049/ptee.1971.0246

16. Lancaster, J., ed. 1986. *The Physics of Welding*, Second Edition. Elmsford, N.Y.: Pergamon Press. DOI: 10.1016/B978-0-08-034076-0.50004-9

17. Eickhoff, S. T., and Eagar, T. W. 1990. Characterization of spatter in low-current GMAW of titanium alloy plate. *Welding Journal* 69(10): 382-s to 388-s.

18. Almeida, P., and Williams, S. 2010. Innovative process model of Ti-6Al-4V additive layer manufacturing using cold metal transfer (CMT). Proceedings of the 21st Annual International Solid Freeform Fabrication Symposium, University of Texas at Austin, Austin, Tex.

19. Lee, T. H., Kang, M., Oh, J. H., and Kam, D.-H. 2022. Deposition quality and efficiency improvement method for additive manufacturing of Ti-6Al-4V using gas metal arc with CMT. *Journal of Materials Processing Technology* 308: 117720. DOI: 10.1016/j.jmatprotec.2022.117720

20. Lee, T. H., Kam, D. H., Oh, J. H., and Kim, C. 2022. Ti-6Al-4V alloy deposition characteristics at electrode-negative polarity in the cold metal transfer-gas metal arc process. *Journal of Materials Research and Technology* 19: 685-696. DOI: 10.1016/j.jmrt.2022.05.030

21. Panchenko, O., Kurushkin, D., Isupov, F., Naumov, A., Kladov, I., and Surenkova, M. 2021. Gas metal arc welding modes in wire arc additive manufacturing of Ti-6Al-4V. *Materials* 14(9): 2457. DOI: 10.3390/ma14092457

22. Rosli, N. A., Alkahari, M. R., Abdollah, M. F. b., Maidin, S., Ramli, F. R., and Herawan, S. G. 2021. Review on effect of heat input for wire arc additive manufacturing process. *Journal of Materials Research and Technology* 11: 2127-2145. DOI: 10.1016/j.jmrt.2021.02.002

23. Ries, D. E. 1983. Gas metal arc welding of titanium. Master of Science Thesis, Massachusetts Institute of Technology.

24. Zhang, Y., and Li, P. 2001. Modified active control of metal transfer and pulsed GMAW of titanium. *Welding Journal* 80(2): 54-s to 61-s.

25. Shinn, B. W., Farson, D. F., and Denney, P. E. 2005. Laser stabilisation of arc cathode spots in titanium welding. *Science and Technology of Welding and Joining* 10(4): 475-481. DOI: 10.1179/174329305X46673

26. Otani, T. 2007. Titanium welding technology. Nippon Steel Technical Report No. 95: 88-92.

27. Kim, Y.-S., and Eagar, T. 1993. Analysis of metal transfer in gas metal arc welding. *Welding Journal* 72(6): 269-s to 278-s.

28. Chae, H., Kim, C., Kim, J., and Rhee, S. 2008. The effect of shielding gas composition in CO₂ laser-gas metal arc hybrid welding. *Proceedings of the Institution of Mechanical Engineers, Part*

B: Journal of Engineering Manufacture 222(11): 1315-1324. DOI: 10.1243/09544054JEM944

29. Smith, L. S., Gittos, M., and Threadgill, P. 1999. *Welding Titanium: A Designers and Users Handbook*. Rotherham, UK: Titanium Information Group; Abington, UK: TWI.

30. Tanaka, M., and Tashiro, S. 2007. A study of thermal pinch effect of welding arcs. *Quarterly Journal of the Japan Welding Society* 25(2): 336-342. DOI: 10.2207/QJJWS.25.336

31. Murphy, A. B., Tanaka, M., Tashiro, S., Sato, T., and Lowke, J. J. 2009. A computational investigation of the effectiveness of different shielding gas mixtures for arc welding. *Journal of Physics D: Applied Physics* 42(11): 115205. DOI: 10.1088/0022-3727/42/11/115205

32. Rao, Z. H., Hu, J., Liao, S. M., and Tsai, H. L. 2010. Modeling of the transport phenomena in GMAW using argon-helium mixtures. Part I - The arc. *International Journal of Heat and Mass Transfer* 53 (25-26): 5707-5721. DOI: 10.1016/j.ijheatmasstransfer.2010.08.009

33. Rao, Z. H., Liao, S. M., and Tsai, H. L. 2010. Effects of shielding gas compositions on arc plasma and metal transfer in gas metal arc welding. *Journal of Applied Physics* 107(4): 044902. DOI: 10.1063/1.3291121

34. Kim, Y., McEligot, D., and Eagar, T. 1991. Analyses of electrode heat transfer in gas metal arc welding. *Welding Journal* 70(1): 20-s to 31-s.

35. Jönsson, P. G., Eagar, T. W., and Szekely, J. 1995. Heat and metal transfer in gas metal arc welding using argon and helium. *Metallurgical and Materials Transactions B* 26(2): 383-395. DOI: 10.1007/BF02660980

36. Kim, C., and Na, S.-J. 2001. A study of an arc sensor model for gas metal arc welding with rotating arc Part 1: Dynamic simulation of wire melting. *Proceedings of the Institution of Mechanical Engineers, Part B: Journal of Engineering Manufacture* 215(9): 1271-1279. DOI: 10.1243/0954405011519321

37. Tsai, N., and Eagar, T. 1985. Distribution of the heat and current fluxes in gas tungsten arcs. *Metallurgical Transactions B* 16(4): 841-846. DOI: 10.1007/BF02667521

TAE HYUN LEE, DONG HYUCK KAM (kamdong@kitech.re.kr), and **CHEOLHEE KIM** (cheol@pdx.edu, chkim@kitech.re.kr) are with the Joining R&D Group, Korea Institute of Industrial Technology, Incheon, South Korea. **LEE** and **JE HOON OH** are with the Department of Mechanical Design Engineering, Hanyang University, Seoul, South Korea. **KIM** is also with the Department of Mechanical and Materials Engineering, Portland State University, Portland, Ore.



Authors: Submit Research Papers Online

Peer review of research papers is now managed through an online system using Editorial Manager software. Papers can be submitted into the system directly from the *Welding Journal* page on the American Welding Society (AWS) website (aws.org) by clicking on "submit papers." You can also access the new site directly at editorialmanager.com/wj. Follow the instructions to register or log in. This online system streamlines the review process and makes it easier to submit papers and track their

progress. By publishing in the *Welding Journal*, nearly 60,000 members will receive the results of your research.

Additionally, your full paper is posted on the AWS website for FREE access around the globe. There are no page charges, and articles are published in full color. By far, the most people, at the least cost, will recognize your research when you publish in the world-respected *Welding Journal*.